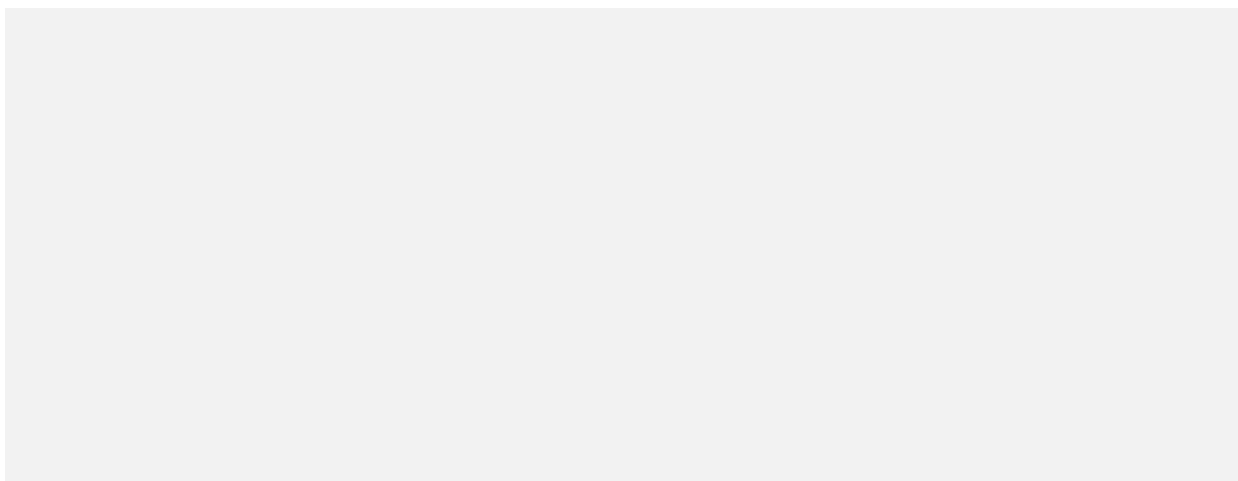


Postprint

This is the accepted version of a paper published in

This paper has been peer-reviewed but does not include the final publisher proof-corrections or journal pagination.

Citation for the original published paper (version of record):



Access to the published version may require subscription.

N.B. When citing this work, please cite the original published paper.

This document is the accepted manuscript version of the following article:
Wilhelm, J., Golze, D., Talirz, L., Hutter, J., & Pignedoli, C. A. (2018). Toward GW calculations on thousands of atoms. *Journal of Physical Chemistry Letters*, 9(2), 306-312. <http://doi.org/10.1021/acs.jpclett.7b02740>

Towards GW Calculations on Thousands of Atoms

Jan Wilhelm,^{*,†,‡} Dorothea Golze,[¶] Leopold Talirz,^{§,||} Jürg Hutter,[†] and Carlo A. Pignedoli^{*,⊥}

[†]*Department of Chemistry, University of Zurich, Winterthurerstrasse 190, CH-8057 Zurich, Switzerland*

[‡]*Present address: BASF SE, Carl-Bosch-Straße 38, D-67056 Ludwigshafen am Rhein, Germany*

[¶]*COMP/Department of Applied Physics, Aalto University, P.O. Box 11100, FI-00076 Aalto, Finland*

[§]*Theory and Simulation of Materials, École Polytechnique Fédérale de Lausanne, Station 9, CH-1015 Lausanne, Switzerland*

^{||}*Laboratory of Molecular Simulation, École Polytechnique Fédérale de Lausanne, Rue de l'Industrie 17, CH-1951 Sion, Switzerland*

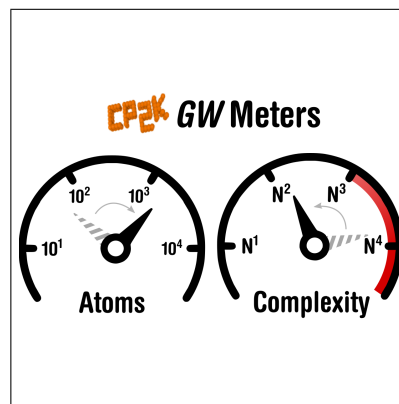
[⊥]*Swiss Federal Laboratories for Materials Science and Technology (Empa), Überlandstrasse 129, CH-8600 Dübendorf, Switzerland*

E-mail: jan.wilhelm@basf.com; carlo.pignedoli@empa.ch

Abstract

The GW approximation of many-body perturbation theory is an accurate method for computing electron addition and removal energies of molecules and solids. In a canonical implementation, however, its computational cost is $O(N^4)$ in the system size N , which prohibits its application to many systems of interest. We present a full-frequency GW algorithm in a Gaussian-type basis, whose computational cost scales with N^2 to N^3 . The implementation is optimized for massively parallel execution on state-of-the-art supercomputers and is suitable for nanostructures and molecules in the gas, liquid or condensed phase, using either pseudopotentials or all electrons. We validate the accuracy of the algorithm on the GW100 molecular test set, finding mean absolute deviations of 35 meV for ionization potentials and 27 meV for electron affinities. Furthermore, we study the length-dependence of quasiparticle energies in armchair graphene nanoribbons of up to 1734 atoms in size, and compute the local density of states across a nanoscale heterojunction.

Graphical TOC Entry



Electronic excitations in nanostructures and at complex interfaces play a decisive role in several key materials challenges, such as energy conversion (1) and digital electronics (2). The *GW* approximation of many-body perturbation theory (3,4) is a method devised for computing the energies of charged excitations, which involve the addition or removal of electrons. It accounts for the non-local, frequency-dependent screening of the interaction between electrons, which is particularly essential where materials vary over electronic length scales. The *GW* spectra can be compared to photoemission spectroscopy and scanning-tunneling spectroscopy, and form the basis for the accurate prediction of optical spectra via the Bethe-Salpeter equation (5). The good performance of the *GW* approximation in predicting band structures of solids and, more recently, ionization potentials and electron affinities of molecules (6) has led to increasing interest from the chemistry community. However, the computational complexity of the canonical *GW* algorithm (7–10) is $O(N^4)$ in the system size N , with a substantial prefactor. This would prohibit the study of many systems of interest, such as solid-liquid interfaces (11), large metal complexes in solution (12), metal-organic frameworks (13), defect states (14) or *p-n* junctions (15,16) that require calculations on hundreds to thousands of atoms.

In recent years, substantial efforts have therefore been devoted to reducing the computational cost of *GW* calculations. The prefactor has been tackled by avoiding the sum over empty states in the polarizability (11,17,18) as well as with a low-rank approximation of the dielectric matrix (11,19). The size of the matrices involved can also be reduced by switching from the traditional plane-wave basis to smaller, localized basis sets (7–9,20,21), which are particularly suited for molecular systems (22–25). Others have tackled the exponent: Foerster *et al.* (26) devised a cubic-scaling *GW* algorithm in a Gaussian basis that exploits the locality of electronic interactions. The method has been applied to molecules with tens of atoms. Liu *et al.* (27) implemented a variant of the cubic-scaling *GW* space-time method (28), using a plane-wave basis, real-space grids and sophisticated minimax quadratures (27,29) in imaginary time and frequency. Its linear scaling with the

number of k -points is particularly promising for applications to large and numerically challenging periodic systems. Finally, Neuhauser *et al.* (30) reported a stochastic *GW* algorithm which nominally enables linear scaling with system size and is straightforward to parallelize. The algorithm has been applied to a silicon nanocluster with one thousand atoms, but further exploration is needed to verify that stochastic *GW* is a useful tool for more complex systems (31).

In this work, we present an efficient low-scaling *GW* algorithm in a Gaussian basis that has been optimized for massively parallel execution on state-of-the-art supercomputers. In comparison to plane waves, the smaller size of the Gaussian basis together with the exploitation of sparsity in two- and three-index tensor operations increase performance while maintaining accuracy, as we demonstrate on the *GW*100 test set (32). The algorithm is suited for nanostructures and molecules in the gas, liquid or condensed phase and is implemented in version 5.0 of the open-source CP2K package (33).

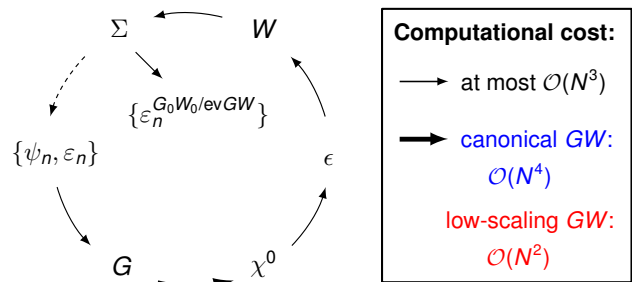


Figure 1: Sketch of *GW* workflow. Regular arrows indicate operations of at most $O(N^3)$ computational complexity. The thick arrow is $O(N^4)$ in canonical *GW* (blue) and $O(N^2)$ in low-scaling *GW* (red). The dashed arrow corresponds to eigenvalue-selfconsistent *GW* (evGW). A detailed flowchart of the canonical and the low-scaling *GW* algorithm can be found in the Supporting Information on page S2.

As sketched in Fig. 1, the *GW* calculation starts from a set $\{\psi_n, \epsilon_n\}$ of single-particle orbitals ψ_n and corresponding eigenenergies ϵ_n . Usually, these stem from a previous Kohn-Sham density functional theory (DFT) calculation, but other starting points, such as Hartree-Fock and hybrid function-

als, are also available.

The orbitals are expanded in the primary Gaussian-type orbitals (GTOs) $\{\phi_\mu\}$

$$\psi_n(\mathbf{r}) = \sum_{\mu} C_{n\mu} \phi_{\mu}(\mathbf{r}) \quad (1)$$

using the molecular orbital (MO) coefficients $C_{n\mu}$.

Following the *GW* space-time method, we proceed to computing the time-ordered single-particle Green's function $G(i\tau)$ in imaginary time:

$$G_{\mu\nu}(i\tau) = \begin{cases} i \sum_n^{\text{occ}} C_{n\mu} C_{n\nu} \exp(\varepsilon_n \tau), & \tau > 0, \\ -i \sum_n^{\text{virt}} C_{n\mu} C_{n\nu} \exp(\varepsilon_n \tau), & \tau < 0. \end{cases} \quad (2)$$

A key step in the algorithm is computing the irreducible polarizability $\chi^0(i\tau) = -iG(i\tau)G(-i\tau)$. (28) Building on previous work (34), χ^0 is obtained in an auxiliary Gaussian basis $\{\varphi_P\}$ (35–37) that is designed to span the product space $\{\psi_i\} \otimes \{\psi_a\}$ of occupied and unoccupied orbitals, and is typically two to three times larger than the corresponding primary basis $\{\phi_\mu\}$. The matrix $\chi_{PQ}^0(i\tau) = \langle \varphi_P | \chi^0(i\tau) | \varphi_Q \rangle$ is calculated as

$$\begin{aligned} \chi_{PQ}^0(i\tau) = & -i \sum_{\mu\sigma} \sum_{\lambda} (\lambda\sigma P) G_{\mu\lambda}(i\tau) \\ & \times \sum_{\nu} (\mu\nu Q) G_{\nu\sigma}(-i\tau), \end{aligned} \quad (3)$$

where the three-center overlap tensors

$$(\nu\mu P) = \int d\mathbf{r} \phi_{\nu}(\mathbf{r}) \phi_{\mu}(\mathbf{r}) \varphi_P(\mathbf{r}) \quad (4)$$

are computed analytically (34).

Since the overlap tensors $(\mu\nu P)$ vanish unless the GTOs ϕ_μ , ϕ_ν and φ_P are centered on nearby atoms, their size grows only linearly with the system size N . The computational cost of Eq. (3) is therefore $O(N^2)$ without the requirement of sparse density matrices or additional localization techniques. The overlap tensor in Eq. (4) can be understood as deriving from the resolution of the identity (RI) with the *overlap metric* (RI-SVS) (38–40). We note that the popular RI with the *Coulomb metric* (RI-V) (38) converges faster with the size of the RI basis, but does not lead to sparsity in (4) and

would thus provide no advantage over the canonical implementation (see supporting information).

Although the cost of the matrix-matrix multiplication in Eq. (2) and all following matrix operations in Eqs. (5), (7), (8), (9) scale cubically with system size, Eq. (3) remains the computational bottleneck even for the largest systems addressed in this work. Therefore, the computation of the polarizability from Eq. (3) has been optimized for massive parallelism (34) using the DBCSR library for sparse matrix-matrix multiplications (41).

We proceed by including the non-orthogonality of $\{\varphi_P\}$ in $\tilde{\chi}^0(i\tau)$,

$$\tilde{\chi}^0(i\tau) = \mathbf{S}^{-1} \chi^0(i\tau) \mathbf{S}^{-1} \quad (5)$$

via the overlap matrix

$$S_{PQ} = \int d\mathbf{r} \varphi_P(\mathbf{r}) \varphi_Q(\mathbf{r}). \quad (6)$$

Following the route of the *GW* space-time method (28), the polarizability $\chi^0(i\tau)$ is transformed to imaginary frequencies via a cosine transform on the minimax grid, (27) and the symmetric dielectric function $\epsilon(i\omega)$ is computed by (42)

$$\epsilon(i\omega) = \mathbf{1} - \mathbf{L}^T \tilde{\chi}^0(i\omega) \mathbf{L} \quad (7)$$

where \mathbf{L} denotes the Cholesky decomposition of the Coulomb matrix \mathbf{V} ,

$$\mathbf{V} = \mathbf{L}\mathbf{L}^T, \quad V_{PQ} = \int d\mathbf{r} d\mathbf{r}' \varphi_P(\mathbf{r}) \frac{1}{|\mathbf{r} - \mathbf{r}'|} \varphi_Q(\mathbf{r}'). \quad (8)$$

For molecules, the Coulomb matrix is computed analytically (43) and for periodic systems numerically by Ewald summation (44), as commonly used in wavefunction correlation methods (45–47). We note that the algorithm supports both aperiodic and periodic simulation cells in the Γ -only approach (42). For periodicity in three dimensions, a correction scheme is available to accelerate the convergence with supercell size (42).

The screened interaction $W(i\omega) = \epsilon^{-1}(i\omega)V = V + W^c(i\omega)$ is split into the bare Coulomb interaction and the correlation contribution, and the latter

is obtained as (42)

$$\mathbf{W}^c(i\omega) = \mathbf{L} \left[\boldsymbol{\epsilon}^{-1}(i\omega) - \mathbf{1} \right] \mathbf{L}^T, \quad (9)$$

where the symmetric, positive definite $\boldsymbol{\epsilon}(i\omega)$ is inverted efficiently by Cholesky decomposition. A cosine transform brings $\mathbf{W}^c(i\omega)$ back to imaginary time.

This completes the ingredients for the GW self-energy $\Sigma(i\tau) = iG(i\tau)W(i\tau) =: \Sigma^x + \Sigma^c(i\tau)$. In the following, we restrict the treatment to GW schemes without orbital updates, such as G_0W_0 and eigenvalue self-consistent GW (ev GW). Computing the quasiparticle energies for N_{GW} orbitals ψ_n then only requires the N_{GW} corresponding diagonal matrix elements $\Sigma_n(i\tau) = \langle \psi_n | \Sigma(i\tau) | \psi_n \rangle$. For reasons of computational efficiency, we compute the diagonal elements directly, yielding the correlation self-energy

$$\Sigma_n^c(i\tau) = i \sum_{\nu P} \sum_{\mu} G_{\mu\nu}(i\tau)(n\mu P) \sum_Q \tilde{W}_{PQ}^c(i\tau)(Q\nu n), \quad (10)$$

where $\tilde{\mathbf{W}}^c(i\tau) = \mathbf{S}^{-1} \mathbf{W}^c(i\tau) \mathbf{S}^{-1}$, and the static exchange self-energy

$$\Sigma_n^x = - \sum_{\nu P} \sum_{\mu} D_{\mu\nu}(n\mu P) \sum_Q \tilde{V}_{PQ}(Q\nu n), \quad (11)$$

where $D_{\mu\nu} = \sum_n^{\text{occ}} C_{n\mu} C_{n\nu}$ and $\tilde{\mathbf{V}} = \mathbf{S}^{-1} \mathbf{V} \mathbf{S}^{-1}$.

The computational complexity of Eq. (10) and (11) is $O(N_{GW}N^2)$, since $(n\mu P) = \sum_{\nu} C_{n\nu}(\nu\mu P)$ vanishes if ϕ_{μ} and φ_P are centered on atoms far apart from each other, introducing sparsity.

In order to compute quasiparticle energies, $\Sigma_n^c(i\tau)$ is transformed to imaginary frequencies by a sine and cosine transform. (27) It is then evaluated on the real frequency axis $\Sigma_n^c(\varepsilon)$ by analytic continuation using a Padé interpolant of $\Sigma_n^c(i\omega)$ (27,32). The G_0W_0 quasiparticle energies $\varepsilon_n^{G_0W_0}$ are obtained by replacing the DFT exchange-correlation contribution v_n^{xc} with the self-energy,

$$\varepsilon_n^{G_0W_0} = \varepsilon_n - v_n^{\text{xc}} + \Sigma_n^x + \text{Re} \Sigma_n^c(\varepsilon_n^{G_0W_0}) \quad (12)$$

and solving Eq. (12) iteratively for $\varepsilon_n^{G_0W_0}$ via Newton-Raphson. For eigenvalue-selfconsistent GW , the quasiparticle energies then replace the

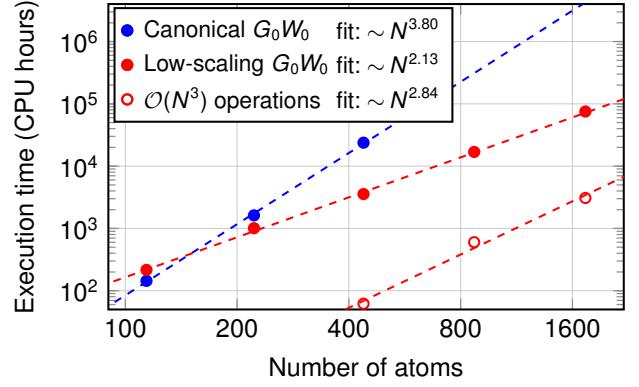


Figure 2: Scaling of G_0W_0 execution time with number of atoms. The canonical algorithm (9) (blue dots) is compared against the low-scaling algorithm (red dots) and its fraction of cubically-scaling operations (red circles). Dashed lines are two-parameters least-squares fits of prefactor and exponent. The systems under study are graphene nanoribbons as shown in Fig. 3. For the largest system containing 1734 atoms, we compute 2883 occupied molecular orbitals and 30195 virtual ones, using 80940 auxiliary basis functions. This calculation was performed on 14400 CPUs on a CRAY XC40 machine.

DFT levels in Eqs. (2) and the GW cycle of Fig. 1 is repeated until self-consistency in the quasiparticle energies $\varepsilon_n^{\text{ev}GW}$ is achieved.

Fig. 2 illustrates how the computational cost of the algorithm scales with the number of atoms N for a technologically relevant test system of graphene nanoribbons, which is discussed in more detail below. The total execution time of the canonical G_0W_0 @PBE implementation (9) (blue) scales with $N^{3.8}$, and constraints in computation time and memory prohibit us from going beyond 500 atoms. The low-scaling algorithm (red) becomes superior between 100 and 200 atoms, is already a factor of 8 faster at 438 atoms than the canonical implementation, and allows to reach much larger system sizes on the same computer architecture (1734 atoms and 5766 electrons in this example).

We stress that the cost of the low-scaling algorithm scales like $N^{2.1}$ with the number of atoms N in the range considered here, since the cubic-scaling steps (red circles) have a much smaller prefactor than the $O(N^2)$ evaluation of Eq. (3) in-

volving sparse tensor operations. In this regime, we expect the algorithm to be particularly efficient for low-dimensional systems, such as 2d materials or 1d polymers and wires, as well as for systems with a local electronic structure, such as molecules in solution, which give rise to sparse density matrices and Green’s functions (48). For very large systems, the cubic-scaling steps will dominate and sparsity becomes irrelevant. By extrapolating the data shown in Fig. 2, we estimate the cross-over from quadratically-dominated to cubically-dominated to occur at $\approx 3 \cdot 10^4$ atoms ($\approx 10^5$ electrons) for the systems under study. For very small systems, all three-center integrals have to be retained and the larger RI-SVS basis puts the low-scaling GW at a slight disadvantage compared to the canonical algorithm using RI-V.

The accuracy of the low-scaling GW algorithm is validated on the $GW100$ set by van Setten *et al.* (32). We compute the energies of the highest occupied molecular orbital (HOMO), or *ionization potential*, and the lowest unoccupied molecular orbital (LUMO), or *electron affinity*, at the $G_0W_0@PBE$ level for all molecules in the set. All values are reported in the Supporting Information on pages S3/S4 and compared to reference values from FHI-aims (7,32), an all-electron code using numerical, atom-centered basis functions. We find that HOMO energies match within 30 meV for 74 out of 100 molecules, while LUMO energies match within 30 meV for 87 molecules.

For comparison, we note that HOMO energies from FHI-aims and VASP (27), a plane-wave code implementing the projector augmented wave method (49), have a mean absolute deviation (MAD) of 60 meV on a subset of $GW100$ (50), while we find a MAD of 35 meV between FHI-aims and our algorithm (on $GW100$ excluding BN, O_3 , BeO, MgO, CuCN and Ne). We conclude that our implementation is suitably accurate and continue by discussing its application to large systems.

We start by studying anthenes, graphene nanoribbons (GNRs) of seven carbon atoms width, as depicted in Fig. 3(a). Recent advances in on-surface chemistry have enabled the bottom-up fabrication of these GNRs with atomic precision (51), and their electronic structure has been investigated in detail by scanning tunnel-

ing spectroscopy (52,53). For these particular GNRs, HOMO and LUMO are found to be localized at the zigzag edges of the ribbons, as depicted in Fig. 3(a), while the remaining frontier orbitals delocalize along the ribbon. One therefore distinguishes the zigzag gap Δ_{zz} between edge-localized HOMO and LUMO states, and the arm-chair gap Δ_{AC} between the delocalized HOMO-1 and LUMO+1, as sketched in Fig. 3(b). Since only the delocalized states are available for charge transport along the ribbon, Δ_{AC} is also termed the transport gap. We compute Δ_{zz} and Δ_{AC} for anthenes containing up to 1734 atoms, see Fig. 3(c) and (d).

As expected from their highly localized nature, and in agreement with previous work (53), the zigzag gap converges quickly with length. First, we note that the converged $G_0W_0@PBE$ value of $\Delta_{zz} = 2.4$ eV is significantly lower than the 2.8 eV reported in Ref. 53, where the frequency-dependence of the polarizability was approximated by a plasmon-pole model. This is in line with findings for molecules in $GW100$ (32) and indicates that plasmon-pole models should be avoided in future studies of localized states in GNRs. Secondly, self-consistency in the eigenvalues leads to a substantial increase of the gap to 3.2 eV. This observation is easily understood by considering that the tiny PBE Kohn-Sham gap of 0.6 eV gives rise to a strong screening of this localized state in the interaction W_0 that is suppressed by the larger GW gap in subsequent self-consistency iterations. Techniques for improving the DFT starting point include the use of hybrid density functionals with adequate fractions of Hartree-Fock exchange (54,55).

The low-scaling algorithm also allows us to study the convergence of the transport gap with GNR length, which requires significantly longer GNRs due to the delocalized nature of the involved electronic states. As shown in Fig. 3(d), the transport gap saturates at a value of $\Delta_{AC} = 3.2$ eV ($G_0W_0@PBE$). Again, this value is significantly smaller than the value of 3.8 eV reported in early $G_0W_0@LDA$ calculations (56) using periodic boundary conditions and a plasmon-pole model. The effect of eigenvalue-selfconsistency, while still substantial, is smaller for the transport gap, leading to a $evGW@PBE$ value of 3.8 eV.

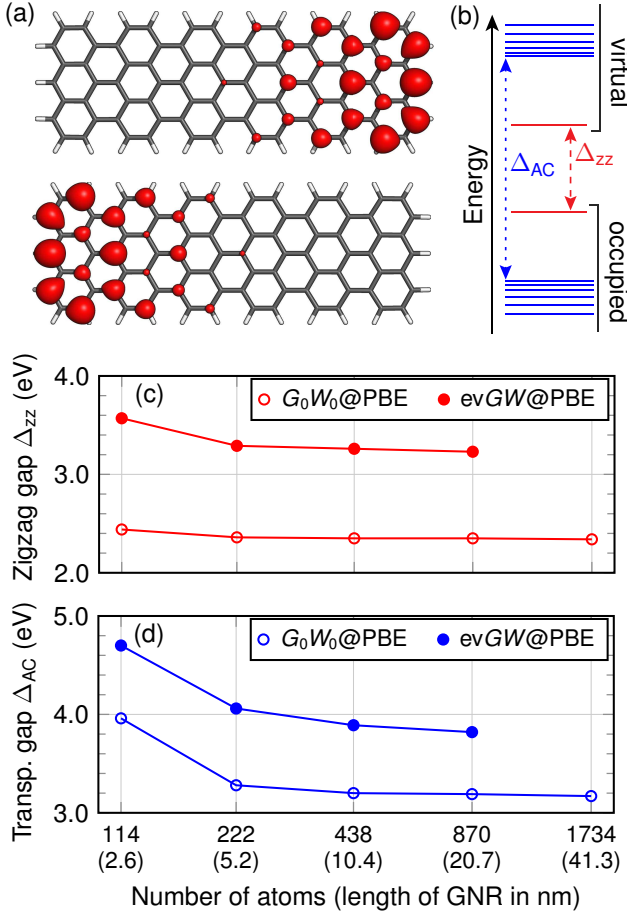


Figure 3: (a) Molecular geometry of 6-anthene together with the zigzag edge states obtained from DFT. All edge carbon atoms are passivated by a single hydrogen atom. Shown in red are iso-surfaces of constant probability density for the HOMO (top) and LUMO (bottom) of the spin-up channel. (b) Sketch illustrating the corresponding spectrum with the HOMO–LUMO gap Δ_{zz} between zigzag (zz) states and the transport gap Δ_{AC} (HOMO-1–LUMO+1) between bulk states. (c) Zigzag gap Δ_{zz} and (d) transport gap Δ_{AC} of anthenes with a horizontal length from 2.6 nm to 41.3 nm.

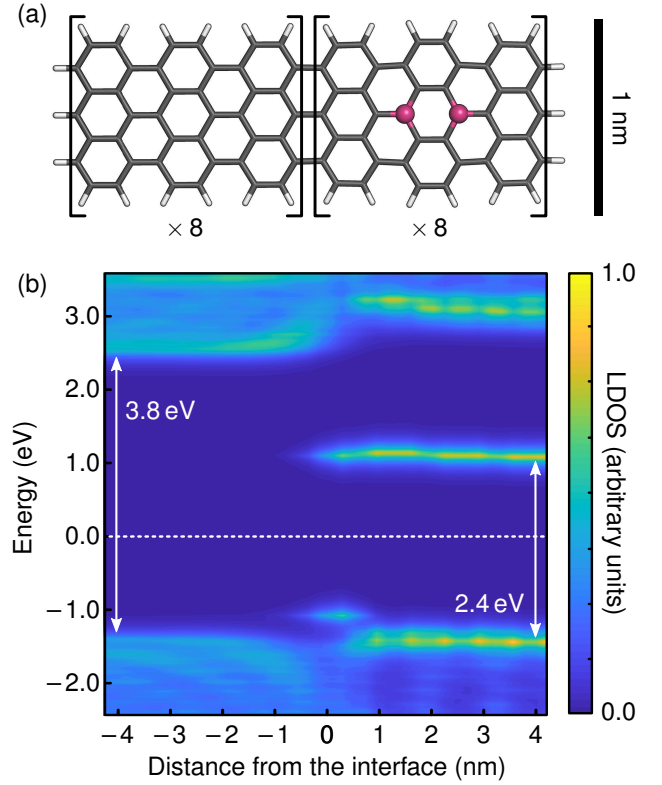


Figure 4: Graphene nanoribbon heterojunction. (a) Atomistic model including 870 atoms (boron dopants shown in purple). (b) Local density of states across the junction based on evGW@PBE eigenvalues, with Gaussian broadening of 0.1 eV and integrated over the plane orthogonal to the GNR axis. The energy zero was chosen as the center of the gap.

In order to enable comparison with experiments (57), where the GNRs are physisorbed on the highly polarizable Au(111) surface, we include the effect of the screening by the substrate via an image charge model devised specifically for the case of GNRs on noble metal surfaces (58). The gap of the pristine GNR reduces by $\Delta_{IC} \approx 1.3$ eV to ≈ 2.5 eV in good agreement with previous experimental and theoretical work (52,53,58).

Next, we turn our attention to heterostructures between doped and undoped GNRs that have recently been demonstrated via on-surface synthesis (15,16,57). The controlled modulation of the band structure and charge carrier concentration through doping, as well as the synthesis of atomically precise heterojunctions are crucial milestones on the path towards graphene nanoribbon electronics. While many-body perturbation the-

ory in the GW approximation is well-equipped to capture the level alignment, energy gaps and local density of states (LDOS) across such interfaces, the long range of the Coulomb interaction can make it necessary to treat large numbers of atoms in order to obtain converged results.

Fig. 4(a) depicts an interface between a pristine GNR and its boron-doped variant, as realized experimentally via bottom-up synthesis in Ref. 15. We perform $evGW@PBE$ calculations for the heterojunction containing 870 atoms, which converges the gap to ≈ 0.1 eV, cf. Fig. 3(d). The LDOS at the interface between pristine and doped side is shown in Fig. 4(b). For the bulk gap on the pristine side, we recover the value of 3.8 eV from Fig. 3(d), while the empty p orbitals of B give rise to a weakly dispersing acceptor band (15), yielding a lower band gap of 2.4 eV for the doped GNR. The LDOS also reveals information specific to the interface: the valence band maxima of the pristine and doped GNR align, making this a type-I (straddling gap) heterojunction. Despite the perfect lattice match, an interface state appears close to the Fermi edge (57), which can introduce backscattering and thus strongly affect the current response of the heterojunction at low bias voltages (59). As pointed out by Cao *et al.* (60), the presence this interface state can be deduced from topological arguments, since the interface is one between a one-dimensional topological insulator ($Z_2 = 1$) on the left, and a trivial insulator ($Z_2 = 0$) on the right.

In summary, we have presented an efficient algorithm for computing quasiparticle energies in the GW approximation, requiring $O(N^3)$ operations and $O(N^2)$ memory. The method is a reformulation of the GW space-time method (28) in a Gaussian basis using sparse linear algebra and minimax grids (27) for imaginary time and frequency. Both G_0W_0 and eigenvalue-selfconsistent GW are supported, using either periodic or aperiodic boundary conditions. We have implemented the algorithm in version 5.0 of the open-source CP2K package (33) and benchmarked its accuracy on the complete $GW100$ set of molecules, finding good agreement with reference implementations. The scalability of the algorithm was demonstrated by computing quasiparticle energies of graphene nanoribbons containing up to 1734 atoms and the spatially resolved local density of states of a graphene

nanoribbon heterojunction. By reducing the cost of computing accurate electron removal and addition energies in nanostructures, molecules and their composites, our work provides yet another stepping stone on the path towards *in silico* materials design.

Computational Methods

For the $GW100$ benchmark set (32), we solve the all-electron Kohn-Sham (KS) equations in the Gaussian and augmented plane waves scheme (GAPW) (61) as implemented in CP2K (33). The molecular orbitals are expanded in a def2-QZVP Gaussian-type basis (32) [Eq. (1)], while GW quantities are expanded in a cc-pV5Z-RI auxiliary basis $\{\varphi_P\}$ taken from the EMSL database (37). For the 17 elements from K to Ne not covered by the cc-pV5Z-RI basis, we constructed a large RI basis containing 124 sets up to I functions. 12-point minimax grids were used in imaginary time and frequency. For the analytic continuation, we construct the Padé approximant on the subset of imaginary frequency points in the interval $i[0, \pm 10 \text{ eV}]$, where $+/-$ applies to virtual/occupied MOs.

For the GNRs, we solve the singlet open-shell KS equations in the Gaussian and plane waves scheme (GPW) (62) using Goedecker-Teter-Hutter pseudopotentials (63). The molecular orbitals are expanded in an aug-DZVP Gaussian-type basis which converges the HOMO-LUMO gap within a few tens of meV, see also Ref. 9. As the auxiliary basis, we employ the corresponding RI-aug-DZVP basis from Ref. 9 which has been generated by optimizing the RI-MP2 energy to match the MP2 energy (35,36). For the GW calculations, atom blocks of basis functions with a Frobenius norm lower than 10^{-11} were filtered (41) to make sparse tensor operations [Eqs. (3) and (10)] efficient. This filter threshold is low enough to affect the G_0W_0 HOMO-LUMO gap of the 6-anthene by less than 0.01 eV. We note that using the same filter threshold for the $GW100$ set results in no filtering at all due to the small size of the molecules, i.e. the GNRs and the molecules are treated equally in this respect. Further information on the choice of the filter threshold can be found in the Supporting Information. Again, we use 12-point minimax grids

in time and frequency. Fig. 4(b) was produced by projecting the LDOS onto the atomic orbitals of the GNR and summing over all nine atoms in a vertical line. In this way, the LDOS is integrated over the plane perpendicular to the ribbon axis.

An exemplary, annotated input file is provided in the Supporting Information on page S6.

Acknowledgement

We thank R. Fasel and P. Ruffieux for helpful discussions and M. J. van Setten for sharing basis sets to perform the GW100 benchmark. Calculations were enabled by the Swiss National Supercomputing Center (CSCS), under projects ID mr2 and uzh1. PRACE project 2016153518 is acknowledged. This research was supported by the NCCR MARVEL, funded by the Swiss National Science Foundation.

Supporting Information

A detailed comparison between low-scaling and canonical $O(N^4)$ -scaling GW in a Gaussian basis including a discussion of the resolution of the identity is given; all values for the GW100 test set, a discussion on choosing filter parameters for sparse tensor operations, an exemplary input file together with basis sets and a discussion on the basis set convergence are reported. This material is available free of charge via the Internet at <http://pubs.acs.org>.

References

- (1) Ping, Y.; Rocca, D.; Galli, G. Electronic excitations in light absorbers for photoelectrochemical energy conversion: first principles calculations based on many body perturbation theory. *Chem. Soc. Rev.* **2013**, *42*, 2437–2469.
- (2) Schwierz, F. Graphene transistors: status, prospects, and problems. *Proc. IEEE* **2013**, *101*, 1567–1584.
- (3) Hedin, L. New Method for Calculating the One-Particle Green’s Function with Application to the Electron-Gas Problem. *Phys. Rev.* **1965**, *139*, A796–A823.
- (4) Onida, G.; Reining, L.; Rubio, A. Electronic excitations: density-functional versus many-body Green’s-function approaches. *Rev. Mod. Phys.* **2002**, *74*, 601.
- (5) Jacquemin, D.; Duchemin, I.; Blase, X. Is the Bethe-Salpeter Formalism Accurate for Excitation Energies? Comparisons with TD-DFT, CASPT2, and EOM-CCSD. *J. Phys. Chem. Lett.* **2017**, *8*, 1524–1529.
- (6) Marom, N. Accurate description of the electronic structure of organic semiconductors by GW methods. *J. Phys. Condens. Matter* **2017**, *29*, 103003.
- (7) Ren, X.; Rinke, P.; Blum, V.; Wieferink, J.; Tkatchenko, A.; Sanfilippo, A.; Reuter, K.; Scheffler, M. Resolution-of-identity approach to Hartree-Fock, hybrid density functionals, RPA, MP2 and GW with numeric atom-centered orbital basis functions. *New J. Phys.* **2012**, *14*, 053020.
- (8) Blase, X.; Attaccalite, C.; Olevano, V. First-principles GW calculations for fullerenes, porphyrins, phthalocyanine, and other molecules of interest for organic photovoltaic applications. *Phys. Rev. B* **2011**, *83*, 115103.
- (9) Wilhelm, J.; Del Ben, M.; Hutter, J. GW in the Gaussian and Plane Waves Scheme with Application to Linear Acenes. *J. Chem. Theory Comput.* **2016**, *12*, 3623–3635.
- (10) Deslippe, J.; Samsonidze, G.; Strubbe, D. A.; Jain, M.; Cohen, M. L.; Louie, S. G. BerkeleyGW: A massively parallel computer package for the calculation of the quasi-particle and optical properties of materials and nanostructures. *Comput. Phys. Commun.* **2012**, *183*, 1269–1289.
- (11) Govoni, M.; Galli, G. Large Scale GW calculations. *J. Chem. Theory Comput.* **2015**, *11*, 2680–2696.

- (12) Evangelisti, F.; Güttinger, R.; Moré, R.; Luber, S.; Patzke, G. R. Closer to Photosystem II: A Co₄O₄ Cubane Catalyst with Flexible Ligand Architecture. *J. Am. Chem. Soc.* **2013**, *135*, 18734–18737.
- (13) Sun, L.; Campbell, M. G.; Dinc, M. Electrically Conductive Porous Metal-Organic Frameworks. *Angew. Chem. Int. Ed.* **2016**, *55*, 3566–3579.
- (14) Walz, M.; Wilhelm, J.; Evers, F. Current Patterns and Orbital Magnetism in Mesoscopic dc Transport. *Phys. Rev. Lett.* **2014**, *113*, 136602.
- (15) Cloke, R. R.; Marangoni, T.; Nguyen, G. D.; Joshi, T.; Rizzo, D. J.; Bronner, C.; Cao, T.; Louie, S. G.; Crommie, M. F.; Fischer, F. R. Site-Specific Substitutional Boron Doping of Semiconducting Armchair Graphene Nanoribbons. *J. Am. Chem. Soc.* **2015**, *137*, 8872–8875.
- (16) Cai, J.; Pignedoli, C. A.; Talirz, L.; Ruffieux, P.; Söde, H.; Liang, L.; Meunier, V.; Berger, R.; Li, R.; Feng, X. et al. Graphene nanoribbon heterojunctions. *Nat. Nanotechnol.* **2014**, *9*, 896–900.
- (17) Umari, P.; Stenuit, G.; Baroni, S. GW quasiparticle spectra from occupied states only. *Phys. Rev. B* **2010**, *81*, 115104.
- (18) Bruneval, F. Optimized virtual orbital subspace for faster GW calculations in localized basis. *J. Chem. Phys.* **2016**, *145*, 234110.
- (19) Giustino, F.; Cohen, M. L.; Louie, S. G. GW method with the self-consistent Sternheimer equation. *Phys. Rev. B* **2010**, *81*, 115105.
- (20) van Setten, M. J.; Weigend, F.; Evers, F. The GW-Method for Quantum Chemistry Applications: Theory and Implementation. *J. Chem. Theory Comput.* **2013**, *9*, 232–246.
- (21) Bruneval, F.; Rangel, T.; Hamed, S. M.; Shao, M.; Yang, C.; Neaton, J. B. molgw 1: Many-body perturbation theory software for atoms, molecules, and clusters. *Comp. Phys. Comm.* **2016**, *208*, 149–161.
- (22) Bruneval, F.; Marques, M. A. L. Benchmarking the Starting Points of the GW Approximation for Molecules. *J. Chem. Theory Comput.* **2013**, *9*, 324–329.
- (23) Körbel, S.; Boulanger, P.; Duchemin, I.; Blase, X.; Marques, M. A. L.; Botti, S. Benchmark Many-Body GW and Bethe-Salpeter Calculations for Small Transition Metal Molecules. *J. Chem. Theory Comput.* **2014**, *10*, 3934–3943.
- (24) Knight, J. W.; Wang, X.; Gallandi, L.; Dolgounitcheva, O.; Ren, X.; Ortiz, J. V.; Rinke, P.; Körzdörfer, T.; Marom, N. Accurate ionization potentials and electron affinities of acceptor molecules III: a benchmark of GW methods. *J. Chem. Theory Comput.* **2016**, *12*, 615–626.
- (25) Rangel, T.; Hamed, S. M.; Bruneval, F.; Neaton, J. B. Evaluating the GW Approximation with CCSD(T) for Charged Excitations Across the Oligoacenes. *J. Chem. Theory Comput.* **2016**, *12*, 2834–2842.
- (26) Foerster, D.; Koval, P.; Sánchez-Portal, D. An $O(N^3)$ implementation of Hedin’s GW approximation for molecules. *J. Chem. Phys.* **2011**, *135*, 074105.
- (27) Liu, P.; Kaltak, M.; Klimeš, J.; Kresse, G. Cubic scaling GW: Towards fast quasiparticle calculations. *Phys. Rev. B* **2016**, *94*, 165109.
- (28) Rojas, H. N.; Godby, R. W.; Needs, R. J. Space-Time Method for *Ab Initio* Calculations of Self-Energies and Dielectric Response Functions of Solids. *Phys. Rev. Lett.* **1995**, *74*, 1827.
- (29) Kaltak, M.; Klimeš, J.; Kresse, G. Low Scaling Algorithms for the Random Phase Approximation: Imaginary Time and Laplace Transforms. *J. Chem. Theory Comput.* **2014**, *10*, 2498–2507.
- (30) Neuhauser, D.; Gao, Y.; Arntsen, C.; Karshenas, C.; Rabani, E.; Baer, R. Breaking the Theoretical Scaling Limit for Predicting Quasiparticle Energies: The Stochastic

- GW Approach. *Phys. Rev. Lett.* **2014**, *113*, 076402.
- (31) Vlček, V.; Rabani, E.; Neuhauser, D.; Baer, R. Stochastic GW Calculations for Molecules. *J. Chem. Theory Comput.* **2017**, *13*, 4997–5003.
- (32) van Setten, M. J.; Caruso, F.; Sharifzadeh, S.; Ren, X.; Scheffler, M.; Liu, F.; Lischner, J.; Lin, L.; Deslippe, J. R.; Louie, S. G. et al. GW100: Benchmarking G_0W_0 for Molecular Systems. *J. Chem. Theory Comput.* **2015**, *11*, 5665–5687.
- (33) Hutter, J.; Iannuzzi, M.; Schiffmann, F.; VandeVondele, J. cp2k: atomistic simulations of condensed matter systems. *WIREs Comput. Mol. Sci.* **2014**, *4*, 15–25.
- (34) Wilhelm, J.; Seewald, P.; Del Ben, M.; Hutter, J. Large-Scale Cubic-Scaling Random Phase Approximation Correlation Energy Calculations Using a Gaussian Basis. *J. Chem. Theory Comput.* **2016**, *12*, 5851–5859.
- (35) Weigend, F.; Häser, M.; Patzelt, H.; Ahlrichs, R. RI-MP2: optimized auxiliary basis sets and demonstration of efficiency. *Chem. Phys. Lett.* **1998**, *294*, 143–152.
- (36) Del Ben, M.; Hutter, J.; VandeVondele, J. Electron Correlation in the Condensed Phase from a Resolution of Identity Approach Based on the Gaussian and Plane Waves Scheme. *J. Chem. Theory Comput.* **2013**, *9*, 2654–2671.
- (37) Schuchardt, K. L.; Didier, B. T.; Elsethagen, T.; Sun, L.; Gurumoorthi, V.; Chase, J.; Li, J.; Windus, T. L. Basis Set Exchange: A Community Database for Computational Sciences. *J. Chem. Inf. Model.* **2007**, *47*, 1045–1052.
- (38) Vahtras, O.; Almlöf, J.; Feyereisen, M. Integral approximations for LCAO-SCF calculations. *Chem. Phys. Lett.* **1993**, *213*, 514–518.
- (39) Schurkus, H. F.; Ochsenfeld, C. Communication: An effective linear-scaling atomic-orbital reformulation of the random-phase approximation using a contracted double-Laplace transformation. *J. Chem. Phys.* **2016**, *144*, 031101.
- (40) Duchemin, I.; Li, J.; Blase, X. Hybrid and Constrained Resolution-of-Identity Techniques for Coulomb Integrals. *J. Chem. Theory Comput.* **2017**, *13*, 1199–1208.
- (41) Borštnik, U.; VandeVondele, J.; Weber, V.; Hutter, J. Sparse matrix multiplication: The distributed block-compressed sparse row library. *Parallel Comput.* **2014**, *40*, 47–58.
- (42) Wilhelm, J.; Hutter, J. Periodic GW calculations in the Gaussian and plane-waves scheme. *Phys. Rev. B* **2017**, *95*, 235123.
- (43) Golze, D.; Benedikter, N.; Iannuzzi, M.; Wilhelm, J.; Hutter, J. Fast evaluation of solid harmonic Gaussian integrals for local resolution-of-the-identity methods and range-separated hybrid functionals. *J. Chem. Phys.* **2017**, *146*, 034105.
- (44) Ewald, P. P. Die Berechnung optischer und elektrostatischer Gitterpotentiale. *Ann. Phys.* **1921**, *369*, 253–287.
- (45) Del Ben, M.; Hutter, J.; VandeVondele, J. Forces and stress in second order Møller-Plesset perturbation theory for condensed phase systems within the resolution-of-identity Gaussian and plane waves approach. *J. Chem. Phys.* **2015**, *143*, 102803.
- (46) Rybkin, V. V.; VandeVondele, J. Spin-Unrestricted Second-Order Møller-Plesset (MP2) Forces for the Condensed Phase: From Molecular Radicals to F-Centers in Solids. *J. Chem. Theory Comput.* **2016**, *12*, 2214–2223.
- (47) Del Ben, M.; Schütt, O.; Wentz, T.; Messmer, P.; Hutter, J.; VandeVondele, J. Enabling simulation at the fifth rung of DFT: Large scale RPA calculations with excellent time to solution. *Comput. Phys. Commun.* **2015**, *187*, 120–129.

- (48) Baer, R.; Head-Gordon, M. Sparsity of the Density Matrix in Kohn-Sham Density Functional Theory and an Assessment of Linear System-Size Scaling Methods. *Phys. Rev. Lett.* **1997**, *79*, 3962–3965.
- (49) Blöchl, P. E. Projector augmented-wave method. *Phys. Rev. B* **1994**, *50*, 17953–17979.
- (50) Maggio, E.; Liu, P.; van Setten, M. J.; Kresse, G. GW100: A Plane Wave Perspective for Small Molecules. *J. Chem. Theory Comput.* **2017**, *13*, 635–648.
- (51) Cai, J.; Ruffieux, P.; Jaafar, R.; Bieri, M.; Braun, T.; Blankenburg, S.; Muoth, M.; Seitsonen, A. P.; Saleh, M.; Feng, X. et al. Atomically precise bottom-up fabrication of graphene nanoribbons. *Nature* **2010**, *466*, 470–473.
- (52) Ruffieux, P.; Cai, J.; Plumb, N. C.; Patthey, L.; Prezzi, D.; Ferretti, A.; Molinari, E.; Feng, X.; Müllen, K.; Pignedoli, C. A. et al. Electronic Structure of Atomically Precise Graphene Nanoribbons. *ACS Nano* **2012**, *6*, 6930–6935.
- (53) Wang, S.; Talirz, L.; Pignedoli, C. A.; Feng, X.; Müllen, K.; Fasel, R.; Ruffieux, P. Giant edge state splitting at atomically precise graphene zigzag edges. *Nat. Commun.* **2016**, *7*, 11507.
- (54) Marom, N.; Caruso, F.; Ren, X.; Hofmann, O. T.; Körzdörfer, T.; Chelikowsky, J. R.; Rubio, A.; Scheffler, M.; Rinke, P. Benchmark of GW methods for azabenzenes. *Phys. Rev. B* **2012**, *86*, 245127.
- (55) Körzdörfer, T.; Marom, N. Strategy for finding a reliable starting point for G_0W_0 demonstrated for molecules. *Phys. Rev. B* **2012**, *86*, 041110.
- (56) Yang, L.; Park, C.-H.; Son, Y.-W.; Cohen, M. L.; Louie, S. G. Quasiparticle Energies and Band Gaps in Graphene Nanoribbons. *Phys. Rev. Lett.* **2007**, *99*, 186801.
- (57) Carbonell-Sanromà, E.; Brandimarte, P.; Balog, R.; Corso, M.; Kawai, S.; Garcia-Lekue, A.; Saito, S.; Yamaguchi, S.; Meyer, E.; Sánchez-Portal, D. et al. Quantum Dots Embedded in Graphene Nanoribbons by Chemical Substitution. *Nano Lett.* **2017**, *17*, 50–56.
- (58) Kharche, N.; Meunier, V. Width and Crystal Orientation Dependent Band Gap Renormalization in Substrate-Supported Graphene Nanoribbons. *J. Phys. Chem. Lett.* **2016**, *7*, 1526–1533.
- (59) Wilhelm, J.; Walz, M.; Evers, F. *Ab initio* quantum transport through armchair graphene nanoribbons: Streamlines in the current density. *Phys. Rev. B* **2014**, *89*, 195406.
- (60) Cao, T.; Zhao, F.; Louie, S. G. Topological Phases in Graphene Nanoribbons: Junction States, Spin Centers, and Quantum Spin Chains. *Phys. Rev. Lett.* **2017**, *119*, 076401.
- (61) Lippert, G.; Hutter, J.; Parrinello, M. The Gaussian and augmented-plane-wave density functional method for ab initio molecular dynamics simulations. *Theor. Chem. Acc.* **1999**, *103*, 124–140.
- (62) Lippert, G.; Hutter, J.; Parrinello, M. A hybrid Gaussian and plane wave density functional scheme. *Mol. Phys.* **1997**, *92*, 477–487.
- (63) Goedecker, S.; Teter, M.; Hutter, J. Separable dual-space Gaussian pseudopotentials. *Phys. Rev. B* **1996**, *54*, 1703.